Remote Sensing of Environment 311 (2024) 114286

Contents lists available at ScienceDirect

Remote Sensing of Environment

journal homepage: www.elsevier.com/locate/rse

On the shoreline monitoring via earth observation: An isoradiometric method

F. Caldareri [a], A. Sulli [a], N. Parrino [a,*], G. Dardanelli [b], S. Todaro [a], A. Maltese [b]

[a] Department of Earth and Marine Sciences, University of Palermo, 90123 Palermo, Italy
[b] Department of Engineering, University of Palermo, 90128 Palermo, Italy

ARTICLE INFO

Editor by: Jing M. Chen

Keywords:
Shoreline
Shoreline extraction method
Sandy beaches
Isoradiometric lines
Sub-pixel resolution

ABSTRACT

Shoreline variations, triggered by climate change, eustatism, and tectonic, drive the coastal landscape evolution over multiple spatial and temporal scales. Among the many different existing coast types, sandy coasts are the most sensitive to coastal erosion and accretion processes and, at the same time, often host valuable anthropogenic assets. The rapid and ongoing evolution of these coastal environments poses challenges for their management, necessitating cost-effective and highly reliable methods for measuring these changes. Many remotely sensed shoreline extraction methods have been proposed in the literature, providing valuable tools for improving coastal management. Even if these methodologies allow the demarcation of the shoreline, its pixelated shape usually requires refinement through subsequent smoothing or vector generalization processes. It is important to note that the position of the thus extracted coastline is not a direct result of a measured physical quantity but rather a product of these refinement techniques. To address this problem, we developed a sub-pixel resolution method for extracting shorelines from remotely sensed images of sandy beaches, leveraging the radiometric signature of the shoreline. Validated through precise Global Navigation Satellite System field surveys for positioning the beach foreshore, this method was successfully applied to three beaches in Sicily, in the central Mediterranean, all exhibiting similar microtidal conditions. Its robust design allows for application across various satellite images, employing a straightforward radiometric interpolation method adaptable to different spatial resolutions. This method would be a valuable tool for coastal managers in detecting and mitigating coastal erosion and developing and maintaining anthropogenic coastal assets.

1. Introduction

Shorelines represent the boundary line between the land and seawater surface and its variations drive the coastal landscape evolution over multiple spatial and temporal scales (Parrino et al., 2023; Srivastava et al., 2023; Malik et al., 2024). Among the different coast types existing worldwide, sandy coasts account for 31% of the world's ice-free shorelines, are characterized by remarkable biodiversity and, often host valuable anthropogenic assets (Luijendijk et al., 2018). These sedimentary bodies form in a particularly dynamic geologic environment, in which the perpetual interaction of sediment, wind, currents, tides, and waves, triggered by climate, tectonic and anthropogenic forcings controls their morphology and extension (Parrino et al., 2022). The anthropological, geological, and ecological value of sandy coasts and their sensitivity to erosional and accretional processes make the accurate delimitation of the shoreline critical to protect coastal areas and improve the designing of the hosted anthropogenic asset (e.g. Bengoufa et al., 2023; Boussetta et al., 2023 and references therein). Despite its seemingly straightforward definition, accurately estimating the exact position and evolution of the shoreline becomes challenging, especially given the rapid and continuous changes occurring in these coastal environments (Pardo-Pascual et al., 2012). In contrast to direct field surveys for shoreline delimitation, remote sensing provides rapid assessments and enables the analysis of historical shoreline positions. With the availability of datasets offering over forty years of global coverage, various remotely sensed shoreline extraction approaches have been developed in recent decades (Almeida et al., 2021; Palomar-Vázquez et al., 2018; Vos et al., 2023 and references therein). These include the band thresholding approach, where a threshold value is determined either through man-machine interaction or by a local adaptive strategy (Otsu, 1979). Another approach relies on classification, which involves clustering the image into land and water pixels and

* Corresponding author.
E-mail address: nicolo.parrino@unipa.it (N. Parrino).

https://doi.org/10.1016/j.rse.2024.114286
Received 19 February 2024; Received in revised form 12 June 2024; Accepted 21 June 2024

defining the boundary line between them as the shoreline (Costantino et al., 2020; Gao, 1996; McFeeters, 1996). Almost all these shoreline extraction methods rely on a pixel-bounded approach resulting in the typical sawtooth-shaped that can only be smoothed subsequently. The pixelated nature of these shorelines mirrors the geometric resolution and grid structure of the processed satellite data. Commonly used in scientific and technical circles, pixel-bounded methodologies demarcate shorelines, yet their inherent pixelation often calls for further refinement through smoothing or vector generalization to reach a pseudo-sub pixel resolution (Douglas and Peucker, 1973; Kass et al., 1988). It is essential to recognize that the resulting coastline position is not a direct outcome of a physical measurement but is derived from these post-processing techniques. While many of these approaches highlight significant interest in remotely sensed shoreline extraction, the radiometric analysis of the water/sediment interface on sandy beaches still needs to be explored. To fill this gap, we propose an innovative method, tailored for images captured in the sun range spectrum, that defines the shoreline in remote sensing observations by a specific radiometric value. The method allows then for characterizing the water/sediment interfaces' radiometric properties, by considering an isoradiometric line to represent the physical shoreline, achieving sub-pixel resolution, surpassing the limitations posed by smoothed pixel-bounded shorelines, which we have demonstrated lack a unique radiometric value. Although isoradiometric lines are derived through linear interpolation, it is important to emphasize that the core principle of the suggested methodology is not interpolation, which could be accomplished by other techniques as well, rather, it is fundamentally rooted in the principle of shoreline isoradiometry. We assessed the strengths and weaknesses of our proposed method by applying it to various satellite products and comparing the outcomes with commonly used pixel-bounded methods. The validation was conducted using Global Navigation Satellite System (GNSS) surveys to position the shorelines accurately. For testing and validation, we chose three distinct natural laboratories along the 1600 km coastline of Sicily Island (central Mediterranean). The selected sandy beaches – Torre Salsa, Balestrate, and Vendicari – represent the island's three main coastal orientations and vary significantly in parameters like sediment supply, sediment size, inland lithology, and the intensity and direction of primary currents and winds.

2. Area of study

To comprehensively define the coastline in sandy environments, it is essential to identify the specific area marking the boundary between emerged and submerged lands. Sandy beaches, sculpted by hydrodynamic and sedimentary processes, are divided into distinct sectors identifiable through cross-beach profiling (Short, 1999). Our study focuses on the beachface or foreshore (Fig. 1) a sector of the beach flanked by the landward side's backshore and the seaward side's nearshore (Walker, 1992). The upper boundary of the foreshore is typically the ordinary berm crest, a depositional feature resulting from wave-driven onshore sediment accumulation (Finkl and Makowski, 2020). The lower boundary is marked by either the Low Tide Terraces (LTTs) or a Ridge. The LTT, an erosional feature, forms from wave interaction with the seabed, while Ridges are elongated, low mounds of beach material aligned parallel or nearly parallel to the shore (Bagnold, 1940). This sandy beach sector hosts the shoreline, which is directly moulded by hydrodynamic processes such as currents, tides, and waves and their interaction with sediments (Masselink and Puleo, 2006). Characterized by seaward-sloping planes and including intertidal environments and habitats. A key characteristic of these beaches is the foreshore slope, which is crucial for differentiating between various beach types. The beach slope varies with wave conditions and the addition or removal of different sediment sizes on the beach face. Generally, the slope angle, measured against a horizontal plane, correlates with grain size: coarser sediments like pebbles or cobbles typically form steeper beach faces than sandy compositions. This difference is due to the greater permeability of coarser sediments (Bascom, 1951) which allows wave run-up (or swash) to percolate down through interstitial spaces, reducing the erosive effect of the run-back (or backwash). During storm conditions, beach slopes tend to flatten as sediment is eroded and carried seaward. However, in the calmer wave conditions post-storm, the beach slope reverts to a steeper angle as material is re-accumulated on the beach. This cycle highlights the dynamic nature of coastal environments, continually reshaped by the interplay of natural forces. The sandy beaches investigated in this work, Torre Salsa, Vendicari and Balestrate, are located along the Sicilian coast (Fig. 2A) and exhibit different geological and morphological characteristics (Todaro et al., 2022). While two of the sites chosen lie in a natural reserve, the third site falls in between two harbour structures. Furthermore, following the classification of wave-dominated beaches given by (Short, 1999) and using the data from the nearest wave buoy located off the coast of Mazara del Vallo (https://www.mareografico.it/en/homepage.html), our study sites fall into the LTT beaches, as they are located in areas partially sheltered from direct wave attack, with deep water waves lowered to an average of 1 m, and especially where the sand is fine to medium.

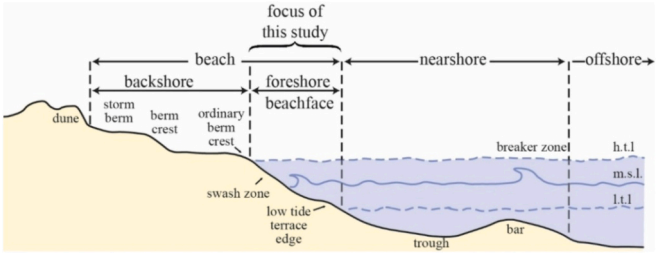

Fig. 1. Different sectors of a sandy beach in cross profile.

2.1. Balestrate beach

The Balestrate beach (38° 2′75" N - 12°58'37" E) is located along the northern coast of Sicily, overlooks the Tyrrhenian Sea and follows an *E*-W direction, (Fig. 2B). It is a 3.2 km long LTT beach composed of sand and gravel of Pleistocene age (F. 593 *Castellammare del Golfo*, CARG project, https://www.isprambiente.gov.it/en?set_language=en) with a typical shoreface slope ranging from 5.22° to 9.25°. Located in the central portion of the Gulf of Castellammare, this beach is bordered to the east by a rocky headland of bio-calcarenites (Marsala Syntem Pleistocene) that ends towards the sea with the harbour structure of Balestrate, while to the west continues with the beaches of Alcamo and Castellammare, which are closed by the homonymous harbour. The main rivers that flow in this coastal sector are named Jato, S. Bartolomeo, besides three ephemeral rivers. The tide regime is microtidal (Astronomical Spring Tidal Range – ASTR - c. 30 cm) with prevailing winds from W and WNW. The resulting longshore current has a W-E direction which generates a solid longshore transport with the same trend. The average beach width is 30 m and a part is occupied by a well-formed system of vegetated coastal dunes.

2.2. Vendicari beach

The Vendicari beach (36°47′27" N- 15°05'53"E), is oriented N-S along the eastern coast of Sicily Island and overlooks the Ionian Sea Fig. 2C). It is a 3.4 km long LTT sandy beach, bordered by two rocky terraces about 10 m high with a typical shoreface slope of 5.14°. The southernmost headland consists of Middle Pliocene calcarenites, while the northernmost beach is part of the equally labelled nature reserve (*Riserva Naturale Orientata Oasi Faunistica di Vendicari)*. The beach is located 4 km south far from the Tellaro river mouth and hosts the mouth of two ephemeral rivers. The tide regime is microtidal (ASTR c. 30 cm) with prevailing winds from the E, *E*-NE, and E-SE, while the most

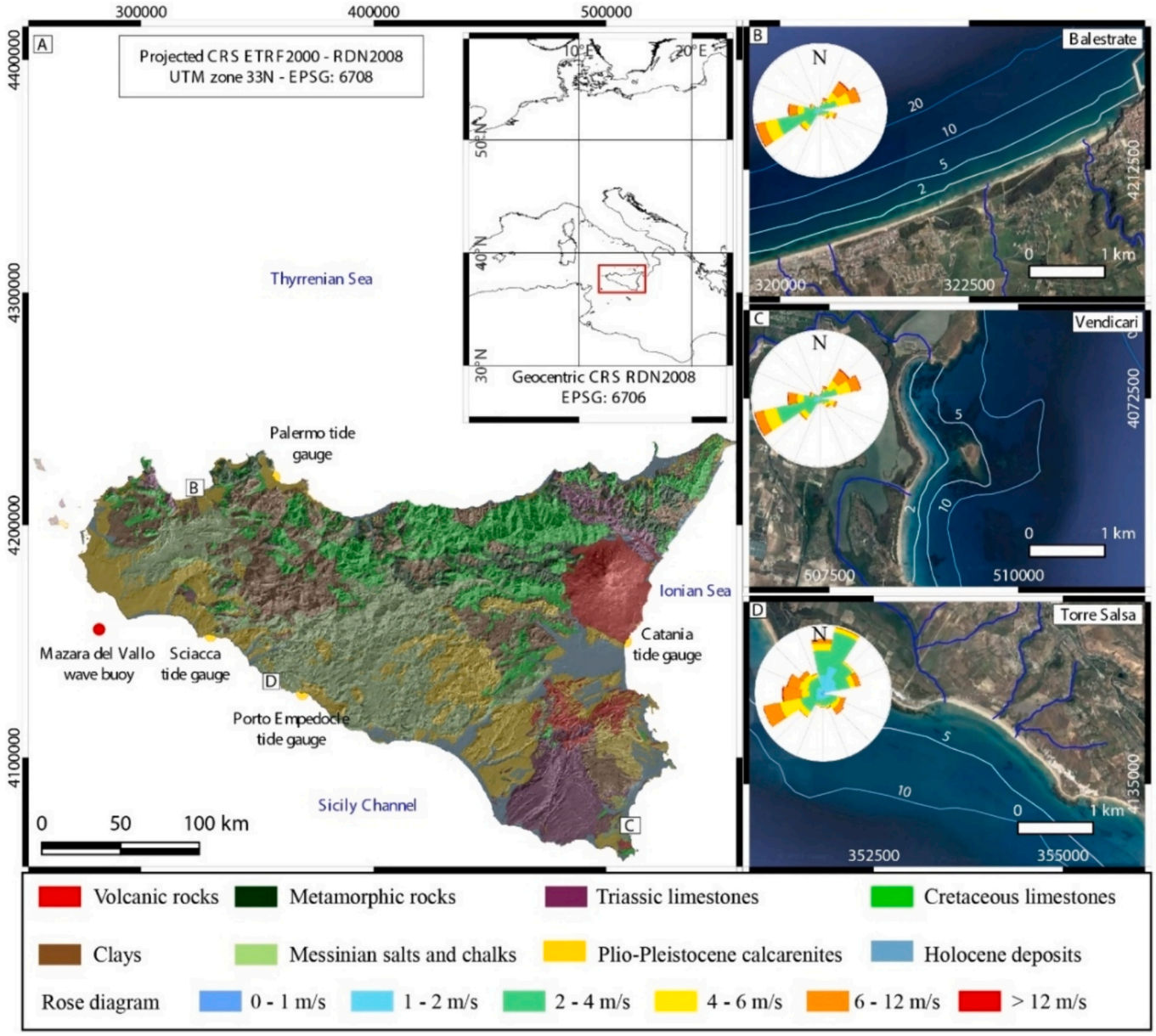

Fig. 2. (A) Lithological chart of Sicily and three study site locations: (B) Balestrate beach, (C) Vendicari beach, and (D) Torre Salsa beach.

frequent and severe storm has significant wave heights >5 m (ISPRA tidal network). The beach is characterized by a longshore current with an N-S direction which generates a solid longshore transport with the same trend. The average beach width is 30 m, and there is a well-formed system of vegetated coastal dunes and a vast marsh behind it.

2.3. Torre salsa beach

The Torre Salsa beach (37°21′53" N - 13°21'15 "E), oriented with a W-NW-E-NE direction, is located along the southern coast of the island and overlooks the Sicily Channel (Fig. 2D). It is a 2.2 km LTT fine sand beach, bordered by two 60 m high headlands, consisting of marly-calcilutites belonging to the Trubi Fm. (Upper Pliocene, F. 636 Agrigento, CARG Project) with a typical shoreface slope of 4.12°. The beach is part of the homonymous nature reserve (*Riserva Naturale Orientata di Torre Salsa*), and there are no coastal defence structures or harbours nearby. About 7.5 km northwest of the beach lies the Platani River mouth, one of the major river networks in Sicily both for its extension and its sedimentary supply. The tide regime is microtidal (ASTR c. 25 cm), with prevailing winds from the W, SW, and SSW (ISPRA tidal network) and most frequent and severe storms approach from the W and WNW with significant wave heights >5 m (ISPRA wave buoy network). Less severe storms approach from the SE, with maximum significant wave heights of 3 m. All these conditions lead to a resulting longshore current with an NW-SE direction which consequently generates a solid longshore transport with the same trend. The average beach width is 40 m, and there is a well-formed system of vegetated coastal dunes in its most internal part.

3. Materials

3.1. Earth observation products

For this study, 3 different Bottom Of Atmosphere (BOA) reflectance bands (near-infrared (NIR), and two shortwave infrareds, SWIR1 and SWIR2), acquired by the Landsat (LS) Operational Land Imager (OLI) images, were selected and tested to compare the accuracy of the extracted shoreline (BOA reflectance is referred to as surface reflectance

- SR). Also, six different spectral bands acquired by the Sentinel-2 (S2) Multispectral Instrument (MSI) ranging from Red Edge (RE) to short wave infrared, and two different spatial resolutions (10 and 20 m) were tested. Within this study, we tested 2 different spectral bands (RE and NIR) acquired by PlanetScope (PS) (Dove and SuperDove sensors) constellation and distributed at 3 m spatial resolution. Satellite products are distributed with cubic convolution resampling. Cubic convolution produces smoother results (thus most continuous) compared to other resampling methods like bilinear interpolation or nearest neighbour (Studley and Weber, 2011; Holmes et al., 2024). However, this smoothness could be considered a limit especially when dealing with sharp radiometric boundaries (Awada et al., 2019).

Among the 3 earth observation products that were tested, two were sensed on the same date, aiming to take advantage of the simultaneity passage of different satellites above the study sites. About the first dataset, S2 and LS-9 images were acquired on 21 July 2022, while two PS images were acquired on 19 and 23 July 2022 on the Balestrate beach. The second one was acquired on 30 July 2022 by S2, LS and PS on Vendicari beach. The third set of satellite images was sensed on 30 August 2022 by S2 and LS and on 29 August 2022 by PS on the Torre Salsa beach. See section 1.1 in Supplementary Materials (SM). The dates of acquisition of the images used to underscore the method's criticalities are documented in the section 5.5. The timeframe for image acquisition was selected to ensure optimal conditions (clear skies and calm seas). To achieve this, various forecasts were consulted, encompassing atmospheric and weather predictions, along with forecasting for wind velocity and direction. Once a suitable period was identified, specific dates were selected based on the scheduling of simultaneous passages of LS, S2, and PS. As reported, this strategy proved successful on the date of July 31st (GNSS acquisition at Balestrate beach) but was not effective on July 21st (GNSS acquisition at Torre Salsa beach) and August 30th (GNSS acquisition at Vendicari beach). In the case of the July 21st acquisition, the PS image was not available on July 20th and 21st. For the acquisition on August 30th, an LS passage was not found. However, considering the tendency for weather conditions to become cloudy in September, it was decided to proceed with the acquisition regardless.

3.2. Global navigation satellite system survey

The GNSS positioning was designed to define the range of the beach where the shoreline is expected to dynamically appear at the moment of the satellite sensing. This range is determined by the positions of the berm and LTT, both of which depend on the daily tidal conditions. The shoreline can be delimitated through different GNSS positioning solutions, including Precise Point Positioning (PPP) and Network Real Time Kinematic (NRTK), besides static and rapid static. To achieve a high-accuracy delimitation we selected a positioning solution suitable to represent the hydrodynamic nature of the process. This involved the use of NRTK for transmitting the differential corrections in real-time. Differential corrections were provided by the Italian GNSS TopNET CORS (Continuously Operating Reference Stations) which is equipped with multi-constellation receivers. Besides constellations, differential corrections are available with different methods, including the Virtual Reference Station (VRS) and Nearest Station (NEA) among others (Dardanelli et al., 2021; Dardanelli and Maltese, 2022). The Italian GNSS CORS is framed in the National Geodetic System ETRF2000 (epoch 2008.0)-*Rete Dinamica Nazionale* (RDN). GNSS tracks used to validate the extracted shorelines in this study are the result of the processing of data acquired using different types of GNSS receivers and RTK instrumental horizontal positioning precisions. During the first campaign, we used three GNSS receivers working with different numbers of constellations to evaluate if the accuracies obtained operating with fewer constellations could achieve appropriate positioning for the case study. See section 1.2 in SM for detailed GNSS receivers' main characteristics.

3.3. Spectroradiometric survey

The spectroradiometric survey was designed to characterize the radiometry properties of the dynamic water-sand system, in the beach-face belt and proximal areas. We employed a FieldSpec® HandHeld spectroradiometer (by Analytical Spectral Device (ASD) Inc., nowadays Malvern Panalytical Ltd). See section 1.3 in SM for a detailed spectroradiometer main characteristics. The spectroradiometer at our disposal does not encompass all the Sun range wavelengths, so it was not possible to characterize the radiometric behaviour of the sand-water column system in the shortwave spectral bands captured by the OLI and MSI sensors and explored in this study.

4. Methods

In this study, we developed a sub-pixel resolution method for shoreline extraction from radiometric beach profiles, demonstrating robust performance with satellite imagery through an isoradiometric approach. The research included evaluations of spectral and spatial resolution accuracy, beach spectral signatures, water depth attenuation, and grain size analysis (See SM Fig. 1 for the detailed workflow adopted in this study). We also compared this method to two established shoreline extraction techniques, identifying key challenges.

4.1. Sedimentologic characterization

The collection of sediment samples aimed to characterize the beach grain size. Samples were collected along cross-beach transects, deemed representative of the entire beach, and in areas with visible macroscopic differences. For each transect, four samples were taken: at the coastal dunes, the beach's middle, the foreshore, and one meter below the water surface. The granulometric analysis, by sieving, was carried out according to the American Society Standard Material (ASTM) D 422/63 standards (ASTM, 2007). The granulometric scale to which the analysed samples refer is the Udden-Wentworth expressed both in D_{50} (median sediment size in mm) and in Φ scale (Terry and Goff, 2014 and references therein). Where Φ is expressed as (1):

$$\Phi = -log_2 \frac{D}{D_0} \tag{1}$$

and D represents the sediment particle size while D_0 *is* the size of a reference sediment particle (usually 1 mm). Furthermore, we computed the foreshore average slope values for the 3 study sites using the equation proposed by (Bujan et al., 2019) as follows (2):

$$tan_\beta = a(D_{50} - 0.125)^b + c \tag{2}$$

where $a = -0.154$, $b = -0.145$ and $c = 0.268$. Using the calculated slope values, we determined the elevation difference for each pixel resolution of the satellite products used. Given that the primary aim of the research was to establish a methodology that could be applied irrespective of field studies, we opted to use an empirical formula that, despite being based on observation and experience, correlates the grain size of the beach with its slope with good approximation. This relationship, well-supported by various studies such as Dean (1991), demonstrates a correlation where the shape parameter increases with the median grain size D50 across different materials allowing us to obtain reliable information compared to punctual sampling (Encyclopedia of Coastal Science, 2020). Although the beach slope could be also characterized via GNSS, during our positioning campaigns, we just delimited the upper limit (ordinary berm) and lower limit (Low Tide level structure, named LTT "Low Tide Terrace"), while we opted not to quantify the slope of the beach face via GNSS.

4.2. Spectroradiometric characterization

To investigate the water/sediment interface definition from a radiometric point of view we performed a field spectroradiometric acquisition characterization, using a visible - near-infrared spectroradiometer, in Torre Salsa beach on 2022-08-30. We carried out 5 punctual measurements spaced about 3 m each, along the beach profile aimed at its spectral signature identification. The spectroradiometer pointed perpendicularly towards the surface under observation, using a bare optical full conical angle field-of-view (25°). Considering that the measurement height was 1.5 m, therefore the resulting footprint on the ground was roughly 65 cm in diameter. Spectral reflectances were calculated by taking the average of 50 repetitions at each measurement point. When the radiance of the target remains stable over time (under clear skies and without any changes in target reflectance), enhancing the number of repetitions aids in maximizing measurement accuracy as errors can be averaged out. The main target was a sandy bottom that exhibited fluctuating reflectance due to variations in water content and water column. To determine the measurement duration and the necessary number of repetitions based on solar radiation, it was essential to monitor the frequency of rising and falling water levels, allowing for multiple observations of this cycle. The spectral reflectance variations due to changes in water content and the water column over the sandy bottom are detailed in the Results/Spectroradiometric findings section. Measurements were also performed on beached *Posidonia oceanica* to discern its radiometric signature from that of the clean beach profile, assessing its impact on remotely sensed shoreline extraction. These measurements were then compared to the BOA reflectance of the satellite products used to identify the spectral signature of the extracted shoreline.

4.3. Shoreline extraction: The proposed isoradiometric method

Following the approach proposed by Maltese et al. (2023, 2024), we evaluated the proposed isoradiometric shoreline extraction method across various spectral bands to identify the most suitable one by quantifying its accuracy and other statistical parameters. We tested the proposed isoradiometric shoreline extraction method on different spectral bands, to determine the more suitable spectral band, by quantifying its accuracy and other statistic parameters. Moreover, we carried out a match between the berm and LTT limits positioned via GNSS, and the shoreline extracted via the proposed isoradiometric method, whose results are shown in chapter 3.4 of SM. Within the GNSS fieldwork path through which we quantified the shoreline extracted points statistical parameters aiming to define which GNSS boundary best approximates the shoreline position. Furthermore, we compared achieved results with those of two of the simplest and most widely used methods in the literature: i) a simple pixel-bounded method that adopts a thresholding approach based on the minimum value between the two histogram peaks as suggested by (Prewitt and Mendelsohn, 1965); ii) a classification method based on the Normalized Difference Water Index (NDWI) and an automated threshold approach. We could have adopted more sophisticated thresholding strategies, such as Otsu's method (1976), which automates threshold selection by minimizing intra-class variance and maximizing inter-class variance. However, to expedite implementation without automation, we selected the minimal value between the two histogram peaks as our threshold. Additionally, we utilized the marching squares algorithm with linear interpolation, as introduced by Cipolletti et al. (2012), for super-resolution segmentation to accurately delineate object borders. This method positions each border point on the linear segment between pixel centres. In their study, Cipolletti et al. applied this technique to delineate the border of a lagoon using LS images, demonstrating that the MSI produces a smooth contour around the lagoon. In computer graphics, marching squares is an algorithm that generates contours for a two-dimensional scalar field. In this study, we extracted isoradiometric lines using the gdal contour utility, which employs linear interpolation of pixel digital values based on the positions of pixel centres. We identified the shoreline position calculating the minimum distance between two consecutive isolines of reflectance. The minimum distance, *H*, between isoradiometric lines is obtained according to the following eq. (3):

$$H_i = \frac{2\$\text{Area}}{\$\text{Perimeter} - 2\text{H}_{i-1}} \quad assuming\ H_0 = 0 \tag{3}$$

where *Hi* is the average distance between two consecutive isolines, the $Area is the area of the narrow polygon delimited by the two consecutive isolines under the hypothesis that that polygon is assimilable to a rectangle with a height almost negligible if compared with the basis, $Perimeter is the perimeter of the polygon whose values is almost equal to twice the basis. The sign $ followed by a field name represents the value of that specific field in the vector layer, to symbolize the creation of new attributes based on existing field values. Since the iterative procedure converges after a few iterations, the calculus was operationally performed by assuming as the distance the value obtained after 5 iterations (for $i = 5$, $H \cong H_i$). We selected as shoreline the isoradiometric line located at the boundary between the two polygons characterized by the lowest values of *H*.

4.4. Comparisons with literature methods

The pixel-bounded thresholding method is a simple straightforward technique and consists of identifying the water/land boundary by thresholding the image based on its histogram values. The approach proposed by (Prewitt and Mendelsohn, 1965) allows the discrimination of pixels having higher and lower values than the threshold: the edge of the two groups of pixels can be thus identified as the shoreline of the examined satellite image band. The NDWI classification method takes advantage of two spectral bands, it consists of a raster calculation applied to the multispectral image to calculate a suitable index, and then, similarly to the previous approach, a thresholding on the NDWI which leads to the binary image whose class limits correspond to the shoreline. According to Gao (1996) and Chen et al. (2005), the NDWI is usually derived using the reflectance ρ in the near-infrared and shortwave bands, $NDWI_G = (SR_{NIR} - SR_{SWIR})/(SR_{NIR} + SR_{SWIR})$. Gao (1996) used the shortwave at 1240 nm, while Chen et al. (2005) used the shortwave at 1640 and 2130 nm. McFeeters (1996) instead, uses the green and the NIR bands, $NDWI_{MF} = (SR_{GR} - SR_{NIR})/(SR_G + SR_{NIR})$. Gao's definition takes advantage of the water absorption at SWIR and can be utilized with S2. However, it is not suitable for the PS dataset which, lacks bands in the SWIR range, despite the advantage of the higher resolution. McFeeters' definition, on the other hand, allows the application even at the PS dataset. We characterized shorelines using a radiometric value, evaluating this through a threshold method. We quantified several statistics, including the count, variability range of isoradiometric curves intercepted, and the average planimetric distance between the first and last intercepted curves. Each statistic was quantified before and after the application of some vector generalization algorithms as implemented in QGIS: a simplification algorithm, the Douglas-Peucker reduction algorithm, hereinafter Douglas algorithm (Douglas and Peucker, 1973;); a smoothing algorithm, the Snake energy minimization algorithm, hereinafter Snakes algorithm (Kass et al., 1988, performed using the default parameters of QGIS).

4.5. Validation: The GNSS delimitation

Designing the GNSS acquisition involves selecting the positioning mode and network correction to ensure high accuracy, crucial for validating the shoreline position as determined from remote sensing. The accuracy of remote-sensed shoreline data varies with spatial resolution and spectral band. The purpose of the GNSS field survey was to validate the shoreline positions extracted from satellite imagery. As we indicate

in the foreshore definition (Fig. 2), we conducted the fieldwork following the ordinary berm crest, identifying as the upper GNSS acquisition limit and the step-in correspondence with the LTT edge as the lower limit. This is because the cyclical nature of the tides tends to create more stable structures since they are constantly modelled by them (unlike the swash-backswash action of the waves which is much more variable), according to the definition of beachface as "the seaward slope of a beach between the low tide line and the upper limit of wave swash" (Finkl and Makowski, 2020). We established a protocol to quantify the accuracy and geometric displacement of the extracted shoreline, conducting operations across three different days—21 July, 31 July, and 30 August 2022—at three study sites representing the southern, eastern, and northern coasts. These dates were chosen to align with the sensing dates of satellite imaging sensors when possible. On the first acquisition day in Balestrate (21 July 2022), three different GNSS receivers were used to assess whether the number of constellations influences the accuracy of GNSS positioning as a benchmark for validating the proposed method and the accuracy of available datasets. In subsequent sessions at Vendicari on 31 July and Torre Salsa on 30 August 2022, a single constellation GNSS receiver was employed. It is to be noted that the Topcon Hiper VR receiver can acquire multiple constellations (including Galileo and Beidu Jin et al., 2022). However, during the research period, the CORS network had not yet been upgraded to offer corrections for all signals, hence positioning solutions relied solely on GPS and GLONASS. The employed GNSS receivers and tracked constellations at each site, plus statistics of the field surveys are reported in section 2.1 of the SM.

4.6. Georeferencing accuracy assessment

To validate the method, we analysed the georeferencing accuracy of the satellite products on an anthropic port structure within the Balestrate harbour. The design of the GNSS acquisition, including the positioning mode and network correction, besides the constellations used to determine the positioning solution, is crucial. Indeed, the accuracy of the GNSS survey needs to be adequate to validate the position estimated with the proposed method. The method's accuracy varies with the spectral bands and the spatial resolution of the dataset. In the study by Dardanelli et al. (2021), the authors quantified some statistics to characterize various positioning modes such as Static, PPP, and NRTK and network correction methodologies (including the Nearest station (NEA), and Virtual Reference Station (VRS) corrections for NRTK, in a different case study). The accurate position of part of the harbour, including a dock, was determined through a GNSS survey using a Trimble R6 receiver. We extracted the position by testing the satellite datasets acquired at a monthly frequency over a span of three years. The test was carried out at different spatial resolutions and spectral bands. For the analysis of georeferencing precision, images were ideally gathered almost monthly from July 2020 to July 2022. The test specifically made use of 30 PS images, 30 S2 images, and 34 LS images. We subsequently evaluated the standard deviation and the average distance between the port structure position extracted and the position obtained via GNSS survey, using four transects placed at regular distances.

5. Results

The first section of results will concern the radiometric elaboration carried out on the clean beach profile; in the second section, the performances of our shoreline extraction method will be determined by comparing the shoreline with the GNSS delimited beachface in terms of accuracy and geometric deviation; the third section it will be shown some method criticalities including the presence of beached *P. oceanica* (other criticalities are widely discussed in section 3.5 of SM) in the fourth section the results will be compared with other methodologies.

5.1. Sedimentology findings

The grain-size analysis allows for determining some beach characteristics. Table 1 shows the D_{50} values both expressed in millimetres and the beach slope, Φ, the mean tidal range and the pixel-related elevation difference for each used satellite product. The D_{50} values show that the beaches have a granulometry which falls within the range of medium-fine sands, except for some portions of Balestrate beach, characterized by medium-sized pebbles. Referring to the 'pixel-related elevation difference' as the difference in elevation along the beach profile, relative to a pixel size. A satellite product with a lower resolution (e.g., LS) will cover a larger elevation difference within a pixel, compared to a higher-resolution satellite product (e.g., PS). Considering that the pixel represents radiometrically the smallest unit of spatial resolution, and that, on sloped surfaces, there exists a height difference within the pixel including the shoreline, with a portion of the pixel being underwater, it could be assumed that the shoreline's resolvability decreases with lower spatial resolution. To estimate the height difference (m) occurring for each pixel which falls along the shoreline, we calculate the slope of the beach profile. The pixel-related elevation difference values increase with the pixel size and range from a minimum of 22 cm for the PS products (3 m resolution) to 4.89 m for the LS products (30 m resolution), highlighting a limit of the low resolution compared to the high resolution. Specifically, the lower resolution is likely to cause a shift in the observed shoreline, a change that's challenging to measure as it depends on the proportion of water coverage and the beach's slope.

5.2. Spectroradiometric findings

The radiometric measurements were performed on the Torre Salsa beach and the obtained values was compared with BOA reflectance values of the satellite images used to identify the extracted shoreline spectral signature. Changes in reflectance over time due to changes in sand water content and the water column are interconnected with the frequency of the water's rise and fall. The reflectance drops periodically as the depth of the water column suddenly increases. Reflectance (Fig. 3A) exhibited a cycle approximately every 6–7 s. Reflectance diminished in the entire spectrum from visible to near-infrared (Fig. 3B) while the water column moved beneath the field of view, ranging between a maximum (over wet sands) and a minimum (while the water column was at its maximum depth over the sandy bottom). This variation was less pronounced in the visible spectrum and more significant in the RE and NIR regions. Beyond 900 nm, the measurements exhibited greater noise.

To calculate the mean value of the spectral reflectance at a specific location, the ~50 repetitions have been averaged over time. The map in Fig. 4, shows a sketch of the Torre Salsa beach with three different grids related to the pixel size of the satellite products used. The base map shows a graduated-coloured scale based on the BOA reflectance values of the PS with a 3 m pixel size. The black grid is related to the 20 m pixel

Table 1
Main beaches' physical and sedimentological characteristics and the elevation difference values related to the different satellite products used (slope of the beach profile according to Bujan's formula D50 (f), Beach slope, S (°), Mean Tidal Range, MTR (m), and satellite products (PS, S2 and LS) elevation difference, ΔH (m).

Site	D_{50} (mm)	D_{50} (f)	S (°)	MTR (m)	ΔH_{PS} (m)	ΔH_{S2} (m)	ΔH_{LS} (m)
Balestrate 1	0.501	0.92	5.22	0.03	0.27	0.91	2.74
Balestrate 2	5.124	−2.105	9.25	0.03	0.49	1.63	4.89
Torre Salsa	0.307	1.583	4.12	0.25	0.22	0.72	2.16
Vendicari	0.482	1.054	5.14	0.20	0.27	0.9	2.7

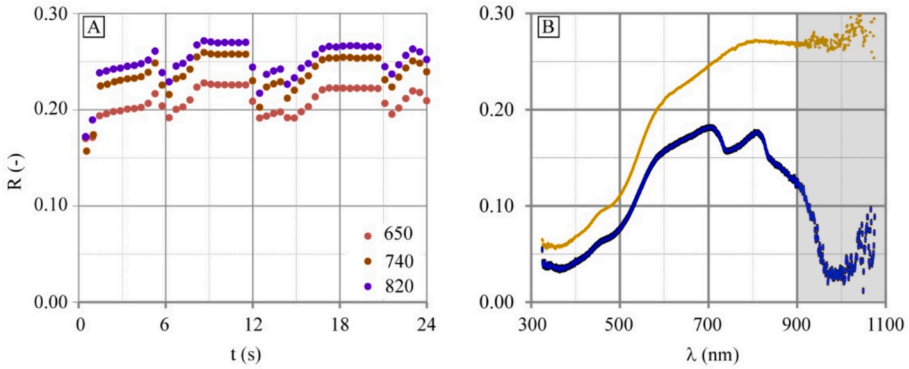

Fig. 3. Variations in reflectance over wet sand (the position nearest to the LTT) on Torre Salsa beach: (a) variation over time (in seconds) in the red (650 nm, represented via red dots), red-edge (740 nm, brown dots), and NIR (820 nm, violet dots) regions; (b) range of variability between maximum (wet sands, represented with a gold line) and minimum (water column over sandy bottom, blue line). (For interpretation of the references to colour in this figure legend, the reader is referred to the web version of this article.)

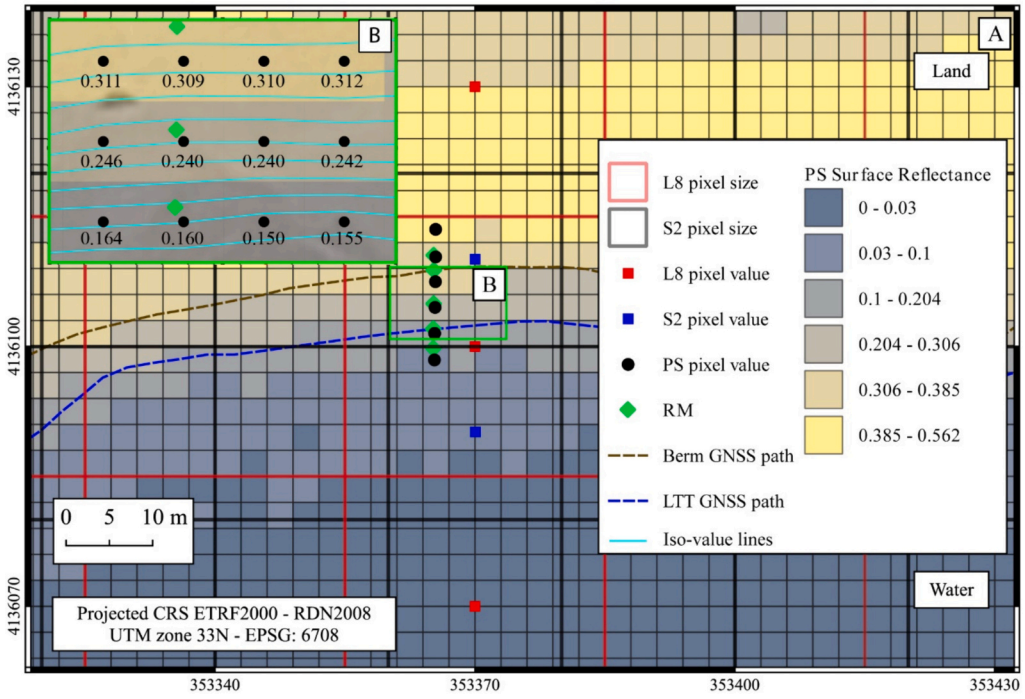

Fig. 4. (A) LS, S2 and PS grids' lines (red squares, black squares and grey squares, respectively, with positions of the spectroradiometric measurements (RM) on Torre Salsa beach; (B) PS images showing the data interpreted as a regular grid of punctual samplings with the contour lines overlapped. (For interpretation of the references to colour in this figure legend, the reader is referred to the web version of this article.)

size S2; the red grid is related to the LS-8 30 m pixel size; the green rhombus represents the localization of the radiometric measurements; the red square, the blue square and the black circles indicate the pixel central position. Results achieved carrying out the field radiometric survey allowed the reconstruction of the radiometric signature of the beach foreshore, extending from the upstream portion of the ordinary berm to the downstream portion of the LTT. In the Torre Salsa case study, this distance ranges from 4.5 to 5.5 m from the berm limit.

We treated the imageries as a regular grid of simultaneous punctual radiometric measurements (Fig. 4B). The interpolation of these punctual measures allows for obtaining radiometric isocontours. We applied a pure linear interpolator, a technique that predicts a value identical to the observed value at its sampling position. Although an inexact interpolator would attempt to achieve a general fit, it would act as a method of smoothing, thereby adding extra levels of abstraction to our methodology. A subset of a PS NIR band interpreted as a regular grid of punctual samplings together with its bimodal distribution is presented in SM Fig. 2. In the NIR, the threshold value is pinpointed in the flat region of the frequency histogram, which is nestled between the two peaks. Since this flat region is also marked by low-frequency values, the pixels neighbouring the threshold line on both sides exhibit (even significantly) different reflectances. Indeed, the threshold method does not identify a line characterized by a chosen threshold; conversely, the interpolation method identifies a line characterized by a given reflectance (the one showing the highest gradient), although it is obtained by interpolated values whose corresponding pixels are not necessarily present in the image.

Fig. 5 shows the spectral reflectances derived from the spectroradiometer measurements. In the x-axis is indicated the wavelength (nm), in a range span from the visible to the NIR; in the y-axis is indicated the BOA reflectance. Fig. 5A refers to the measurements carried out along the clean beach profile and linearly averaged every 3 m (to mimic the

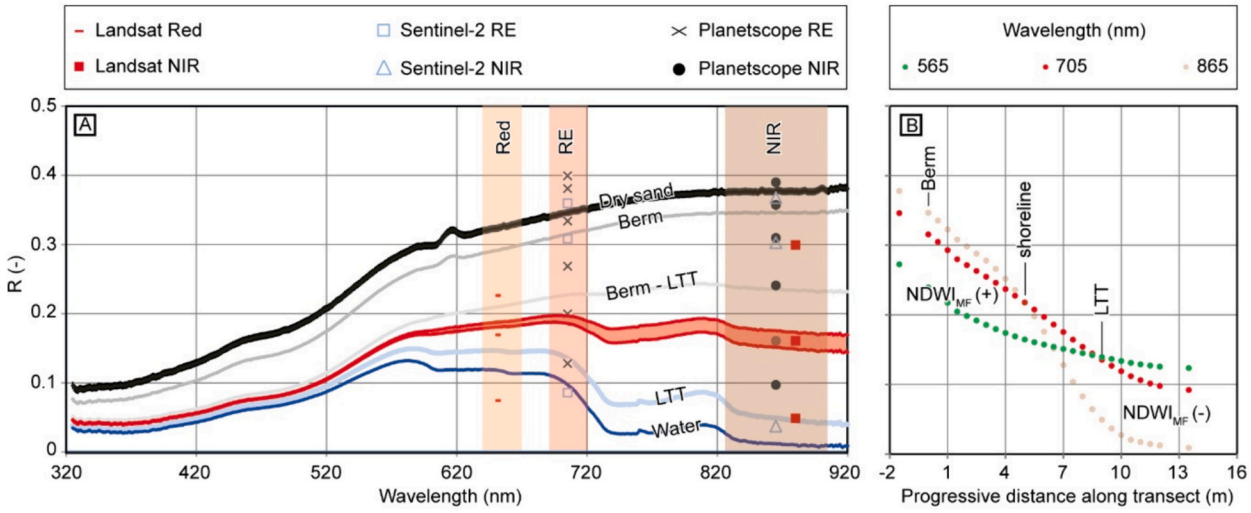

Fig. 5. Spectral signature of Torre Salsa beach. (A) clean beach profile; (B) Trend graphs of the NIR, RE and Green trend along the transect. The measure points of the curves are shown as green rhombus in Fig. 4. (For interpretation of the references to colour in this figure legend, the reader is referred to the web version of this article.)

behaviour of the highest spatial resolution satellite images available). The curves represent the spectral signatures of the different beach portions, starting from the dry sand up to one meter away from the coastline. Black, dark grey and light grey curves have a similar trend and represent respectively dry sand, berm and half the distance between the berm and the LTT. These curves have an increasing trend between 320 and 600 nm, have a peak around 620 nm, and then continue with a weakly increasing trend up to 920 nm. Light blue and dark blue curves represent the spectral signature of the water edge and the water respectively. These have a similar trend and grow from 320 to 590 nm, have a decreasing trend from 590 to 600 nm, a trend that is horizontal up to 695 nm, a descending portion from 695 to 740 nm, a slightly increasing trend up to 810 nm and a further decreasing trend up to 920 nm. The light red area between the two curves was obtained from interpolation to represent where the spectral signature starts showing a spectral signature like the water one. The coloured vertical bands represent the bandwidth of red, RE and NIR respectively. The point symbols represent the BOA Reflectance values obtained on the red, RE and NIR bands in the PS, S2 and LS-8 satellite images, extrapolated along a transect that approximates the radiometric measurements performed in the field (Fig. 4).

Fig. 5B graphs report in the x-axis the progressive distance (m) along the beach and in the y-axis, the SR values considering the PS satellite product. The brown curve represents the trend of the SR considering the NIR wavelength (865 nm); the red curve represents the SR considering the RE wavelength (705 nm). Finally, the green curve represents the SR considering the Green wavelength (565 nm). This graphs can be considered as an expression of the $NDWI_{MF}$. Indeed, it is possible to identify 2 areas:

- the first one, ranging from −1.5 to 6.5 m, in which the $NDWI_{MF}$ assumes positive values;
- the second one, ranging from 6.5 to 12 m, in which the $NDWI_{MF}$ assumes negative values.

The graph in Fig. 8 shows the irradiance values (x-axis) changing with water depth (y-axis), allowing estimating the emerging irradiance from the water surface, assuming a 30 cm bottom depth, because of the surface refraction processes, downward and upward water column attenuation and bottom reflection process.

To perform this calculation, the knowledge of the diffuse attenuation coefficients (K_D) in the NIR and RE wavelengths is required, as well as the Bottom Reflectance (R_B). The K_D value was estimated by comparison with previous acquisitions in Mondello beach and Stagnone di Marsala lagoon (Dardanelli et al., 2021) by comparison at 490 nm with a K_D product derived from OLI/LS 8 at 4 km resolution at Torre Salsa for 29 August 2022 which shows that the value is very similar (slightly higher) to the value measured in Mondello (Maltese et al., 2008). By assuming that the ratio of chlorophyll, suspended solids and yellow matter remained unchanged, the value was interpolated in the NIR and RE. This occurs in instances where there are no alterations in the water's characteristics, such as in the aftermath of flood flows. Regarding the RB, we took the maximum values of saturated sand in the NIR and RE measured during the Torre Salsa radiometric survey of 31 August 2022. Indeed, by analysing the radiometric signatures on the lower part of the foreshore, periodically the reflectance decreases to a minimum (maximum water column during the spectral measurement) or rises to a maximum (when the sand remains without water above during the downward flux). With these assumptions, about 5% of the irradiance escapes from the water column. If we calculate this value, considering a different height of the water column, we obtain different % values of irradiance emerging from the water column (Fig. 6A). Therefore, we determined the approximate height of water where it could be assumed that the method delimits the shoreline. This is because an altimetric uncertainty linked to the penetrability of the irradiance in the water column corresponds to a planimetric uncertainty linked to the slope of the shoreline. The data obtained from the Porto Empedocle tide gauge (see Fig. S1 available as supplementary material) shows that there was a 5–8 cm high tide during the acquisition. Moreover, data from the Mazara del Vallo buoy shows that, although offshore, the spectral significant wave height was about 17 cm (see Fig. S2 available as supplementary material). Therefore, with all the relevant assumptions, we probably had at the LTT, a water column varying between 0 and about 25 cm. If the pixel were infinitesimal, in any case, there would be a vertical uncertainty related to the penetrability of the irradiance in the water, which would turn into a horizontal uncertainty related to the slope of the foreshore. If we assume a vertical uncertainty of 25 cm we have a horizontal uncertainty for our slope already equal to the PS pixel size.

5.3. Isoradiometric shoreline comparison with beachface

Once we radiometrically investigated the shoreline, we applied our sub-pixel extraction method on different satellite image bands. Fig. 7 shows a sketch concerning the elaborations made on the PS NIR band

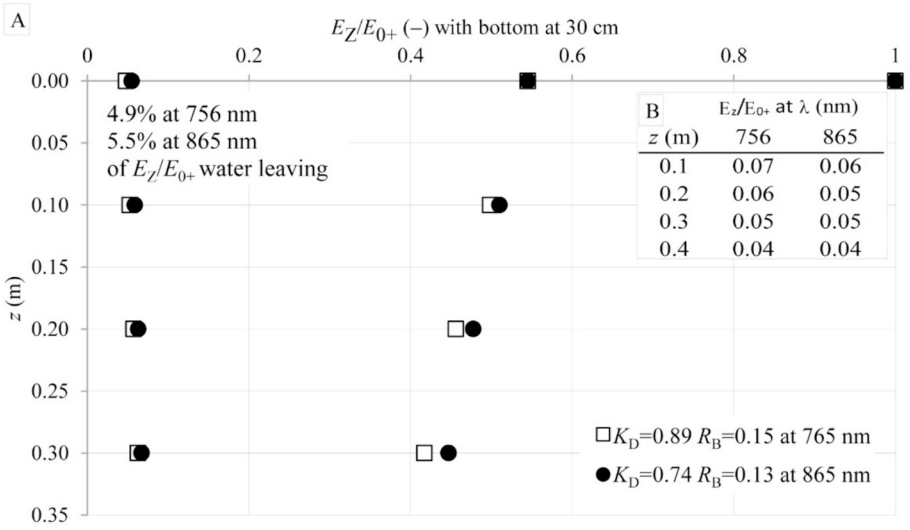

Fig. 6. (a) Spectral irradiance with water depth. K_D (diffuse attenuation coefficients) and R_B (Bottom Reflectance); (b) Irradiance emerging from the water column as a percentage of the downwelling irradiance incident at the water surface, with different water depths.

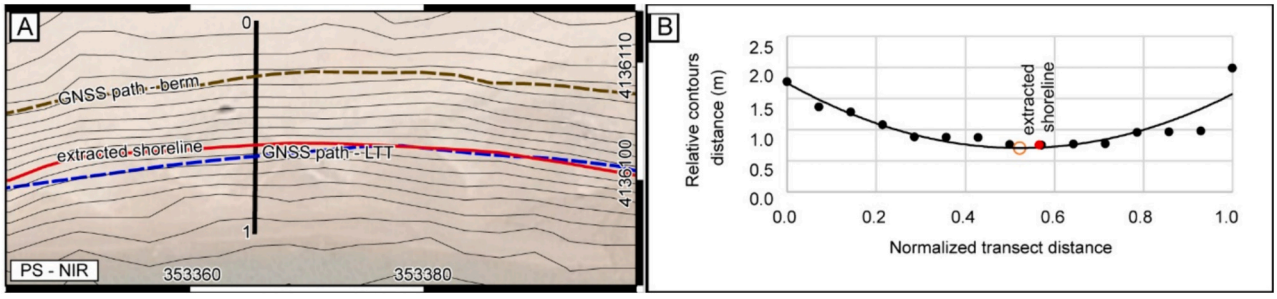

Fig. 7. (A) Radiometric isocontours on PS NIR reflectances (black lines), the dashed brown line is the upper limit (berm) and the dashed blue line is the lower limit (LTT) of the GNSS delimitation. (B) distances between adjacent contours (black dots) and the shoreline position (red dot) for different sensors and bands. (For interpretation of the references to colour in this figure legend, the reader is referred to the web version of this article.)

(other applications performed on different bands of PS, S2 and L8 are available in SM, Fig. 3). Black lines represent the contours of the extracted SR values, and the dashed brown line is the upper limit (berm) and the dashed blue line is the LTT lower limit of the GNSS validation path performed. The Graphs show on the x-axis the normalized transect distance and on the y-axis the relative contours distance. The red point indicates the minimum distance value which corresponds to the shoreline position. The orange circle is the minimum value obtained by processing the interpolated line equation of the curve. Other sketches for different products and bands are reported in section 3.2 of SM.

We then compared the shorelines extracted with the GNSS fieldworks on three study sites to quantify: i) the suitability of GNSS receivers acquiring different numbers of constellations to validate the delineated shorelines; ii) extracted shorelines accuracy; iii) quartile test on PS best performing spectral bands. Specifically, concerning point i), the NRTK GNSS positions were used as a benchmark against remote sensing estimates, under the assumption that these latter would have been less accurate.

5.4. Shoreline accuracy assessment through GNSS beachface delimitation

The range within which the shoreline's position should fall, given its (hydro)dynamic nature, has been delimited via a GNSS survey. The survey was a roundtrip to delimit both the berm and the LTT covering about 6400 m. The satellite acquisition was temporally centred on the GNSS survey. Regarding the definition of shoreline, it's important to note that the shoreline that can be mapped by remote sensing is a radiometric entity. Thus, the premise of the proposed method is that the mappable shoreline via remote sensing is an isoradiometric line. This assumption remains valid as long as the optical properties of the water column and the seabed remain unchanged spatially. Table 1 summarizes the accuracy and main statistics parameters (mean error (μ) and standard deviation (σ)) obtained from the GNSS acquisition using three different GNSS receivers (Trimble R6 - GPS constellation signal, Topcon Hiper V - GPS and GLONASS, Topcon Hiper VR - GPS, GLONASS, and GALILEO). The accuracy represents the percentage of points extracted from the shoreline, which fall within the GNSS limits. Mean error represents the averaging obtained from the points outside GNSS limits and is used to quantify the bias of the extracted shoreline. Table 2 provides insights into the accuracy associated with the features of satellite products (spatial resolution and spectral band), and related to single or multiple constellations. It needs to be highlighted that although the multiple constellations potentialities of the Topcon Hiper VR receiver, in the tested area the CORS was enabled to send the corrections only for GPS and GLONASS, thus the potentialities of the multiple constellations remained unexpressed. For instance, for the same satellite product and analysed band, the differences range from a minimum of 0.38% to a maximum of 12.31% in accuracy. It is shown that, generally, the highest spatial resolutions the best is the matching between extracted shoreline with GNSS positioned foreshore beachface limits, ranging from a minimum of 1.62% for the LS SWIR band to a maximum of 79.18% for the PS RE band. Regarding spectral bands RE and NIR bands perform better than SWIR bands. Finally, no clear improvements are achieved by employing GNSS receiving multiple constellations. For this reason, the

Table 2
Accuracy and main statistics parameters of Balestrate beach extracted shorelines. The band contours interpolation method was applied on the different bands of the PS satellite images sensed on 19 and 23 July 2022 and S2 and LS 9 sensed on 21 July 2022.

year	day/month	sensor	Band number	Central wavelength (nm)	Bandwidth (nm)	R_S (m)	Trimble R6 Accuracy (%)	Topcon Accuracy (%)	Topcon Hiper V Accuracy (%)	Trimble R6 μ (m)	Topcon μ (m)	Topcon Hiper V μ (m)	Trimble R6 σ (m)	Topcon σ (m)	Topcon Hiper V σ (m)
2022	21/07	L8 OLI	5	*865*	*30*	*30*	38.55	35.59	43.99	1.45	1.54	1.52	1.11	1.16	1.29
			6	*1610*	80	30	6.96	6.29	7.05	4.27	4.45	4.12	2.10	2.15	2.06
			7	*2200*	180	30	1.90	1.62	2.09	7.59	7.78	7.42	2.70	2.74	2.67
		S2A	*5*	*704.1*	*15*	*20*	0.00	0.00	0.00	5.86	6.07	5.68	1.85	1.81	1.82
			6	*740.5*	*5*	*20*	70.76	67.05	74.86	0.85	0.86	1.03	0.88	1.00	1.35
			7	*782.8*	*20*	*20*	68.86	65.90	72.40	0.89	0.88	1.02	0.74	0.77	1.09
			8	*832.8*	*106*	*10*	56.83	58.55	60.74	0.91	0.97	1.05	0.79	0.80	0.98
			8A	*864.7*	*21*	*20*	69.34	67.34	72.59	1.10	1.08	1.27	0.93	0.98	1.27
			11	*1613.7*	*91*	*20*	47.09	42.31	54.44	1.00	1.06	1.12	1.01	1.06	1.38
			12	*2202.4*	*175*	*20*	17.56	15.55	19.56	2.17	2.33	2.09	1.17	1.21	1.17
	19/07	PS SuperDove	*7*	*705*	*15*	*3*	77.38	77.76	79.18	1.44	1.46	1.65	1.36	1.31	1.44
			8	*865*	*40*	*3*	67.65	67.75	69.74	1.05	1.10	1.21	0.88	0.83	1.06
	23/07		*7*	*705*	*15*	*3*	57.45	57.17	61.73	1.24	1.22	1.37	1.35	1.35	1.55
			8	*865*	*40*	*3*	70.38	70	70.76	1.05	1.06	1.18	0.96	0.93	1.14

worst performances — best performances

GPS constellation receiver was employed for the test in the other two study areas (Table 2 and SM section 3.3).

Results in Table 2 suggest that a receiver using a single constellation in NRTK mode is adequate for verifying the positioning of the shoreline, which is achieved with the highest accuracy through the isoradiometric method (PS NIR bands, see Section 5.4.1 for details "). Accuracy and main statistics parameters of Torre Salsa and Vendicari beaches extracted shorelines are reported in SM Tables 5 and 6. To assess the

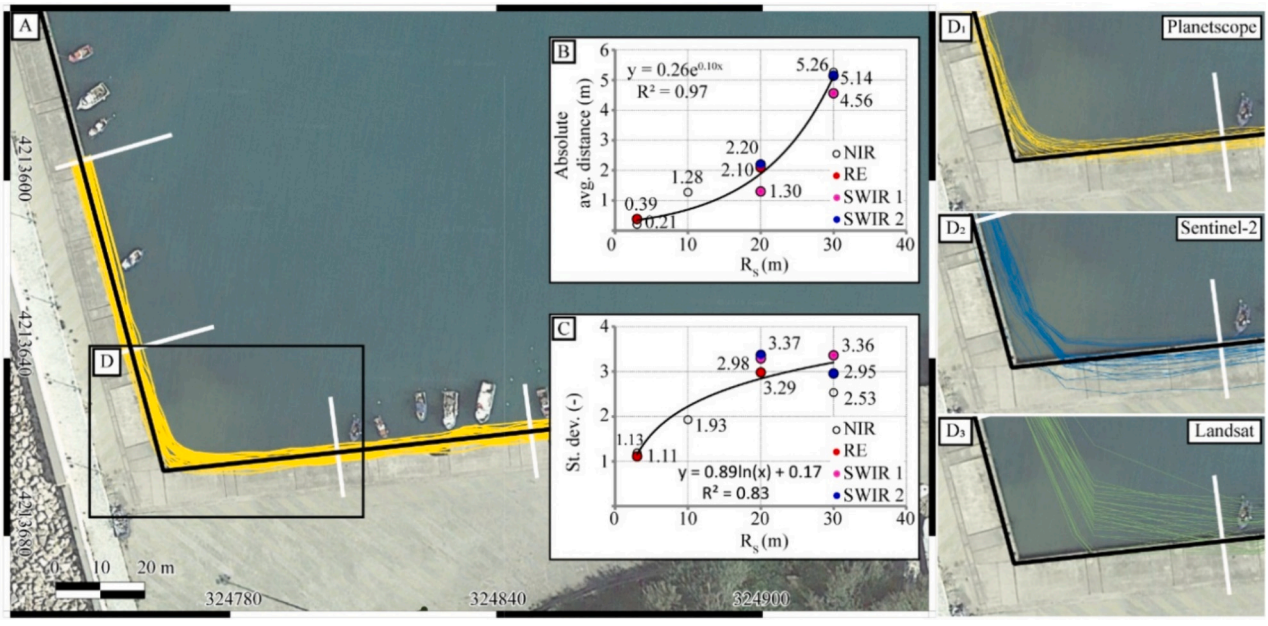

Fig. 8. Georeferencing accuracy validation performed on Balestrate dock structure. (A) satellite images with the detected GNSS position (black line), the remotely sensed extracted dock lines using the PS NIR band (yellow line) and the transect (white line); (B) and (C) show the average distance and the standard deviation graphs with changing spatial resolution. (D) extracted line trends using the 3 different satellite products: D_1: PS; D_2: S2; D_3:LS. (For interpretation of the references to colour in this figure legend, the reader is referred to the web version of this article.)

average performance as well as the performance consistency of different receivers, we evaluated the mean and standard deviation of some metrics reported in Table 2 (namely the accuracy and mean error, SM Table 7, see also SM 3.3).

5.4.1. Georeferencing accuracy validation

A validation of the images' georeferencing accuracy as distributed by the providers was performed on a dock of the harbour of Balestrate by measuring accurately its position via an NRTK survey. The dock delimitation was then compared with those extracted from satellite products. Assuming that the dock is almost stable in time, we delimited the dock on three years of monthly images (one per month). Statistically, each delimitation represents a repetition of a measurement sample, thus allowing the dataset to be viewed as a sample from a data population, that can be processed to characterize the absolute average distance and the standard deviation from the GNSS delimitation assumed as the "true" position. Although being a convenient test from a geometric point of view, we discriminate concrete dock and deep water, while in the operational case studies, we discriminate sand and shallow water which are characterized by different spectral reflectances. A satellite image of the Balestrate dock is shown in Fig. 8A, where the GNSS delimitation is highlighted in black line (reference line). The remotely sensed dock lines are extracted using the NIR band of PS are highlighted in yellow and are assumed as repetitions of the measurements' sample, Finally, the transects used for quantifying the accuracy are highlighted in white. Frame B shows a graph which has the x-axis spatial resolution of the bands adopted and, on the y-axis, the average distance values between the GNSS detected dock position and the one extracted from the satellite products. Higher resolution bands have lower mean distance values, which therefore translates into a more accurate position than the true position. At lower resolution, on the other hand, NIR values are higher than those of the SWIR bands. This is a trend that deviates from what we expected but should not be alarming. Frame C shows a graph which has on the x-axis the spatial resolution of the different bands we used and, on the y-axis, the standard deviation between the multiple lines extracted by remote sensing. The dots in different colours indicate the standard deviation values of the different bands used (NIR, RE, SWIR1 and SWIR2). For the PS's high resolutions, the deviation values are lower for the NIR band than for the RE (1.09 vs. 1.15 m). The NIR band of the S-2 has a value of 1.93 m on the NIR band. The 20 m bands of the S-2 have a value of 3.02, 3.29 and 3.37 m for the RE SWIR1 and SWIR2. The 30 m resolution bands of the LS 8 show a trend that differs from what is expected as a value of 3.23 m is obtained for the NIR which is less than the SWIR1 (3.36 m) but is greater than the SWIR2 (2.95 m).

The test highlights a limit of extracting the shoreline via radiometric interpolation. Indeed, the method cannot describe abrupt direction changes although natural shorelines, and particularly sandy beaches, are characterized by gentle changes in direction, and these abrupt changes often characterize man-made structures. Generally, as the spatial resolution decreases, the perceived shoreline's displacement increases (Fig. 8B). Although an exponential trend line best fits the behaviour of the absolute average distance with spatial resolution, a linear trend line would describe an absolute average distance being roughly 14% of the resolution ($R^2 \cong 0.83$).

5.5. Method criticalities

During Torre Salsa fieldwork we performed radiometric measurements on beached *P. oceanica* aiming to check if the *P. oceanica* hampers the shoreline extraction. Fig. 9 shows the spectral behaviour of dry sand, wet sand, wet *P. oceanica* and water, with wavelengths (nm) and SR reported in the x and y axes respectively. Black curves represent the average spectral reflectance, blue curves represent standard error; noisy spectral bands are highlighted with a grey band. Frame A represent the dry sand spectral signatures. The curve has an increasing trend from 300 to about 800 nm and then continues with a weakly increasing trend. Frame B represents dry *P. oceanica* spectral reflectance: the curve has a low increasing trend from 300 to 700 nm where, a knee point, makes the curve a highly increasing trend to about 900 nm. Frames C and D report the spectral reflectance of a beached wet *P. oceanica* and that of the water breaking on it, showing similar spectral behaviour.

At Vendicari beach, masses of decomposing leaves on beaches led to inaccuracies in the shoreline's positioning. This error was not related to the image georeferencing accuracy, which we had previously verified. Other method criticalities are reported in Section 3.5 of SM, including topographic shadows, the presence of bodies of water behind the beach, and other surface effects including internal waves, clouds not in the scene but partly shadowing the sea and beach, surface turbidity fronts, breaking waves on the shoreline and capillary waves.

5.6. Comparing accuracy with some widespread methods

After we applied and explored the limits of our methods and performed an accuracy assessment, we proceeded with a comparison with interpolation and thresholding methods applied to two different NDWI formulations (Fig. 10). The test was carried out on PS (McFeeters, 1996) and S2 (Gao, 1996) images. The depiction of the shorelines has been magnified in relation to an inset placed near the promontory and another inset in the middle section of the beach.

The performance of the methods has been quantified through the following statistics (Table 3): the proportion of shoreline that falls within the LTT-berm, along with the mean distance and standard

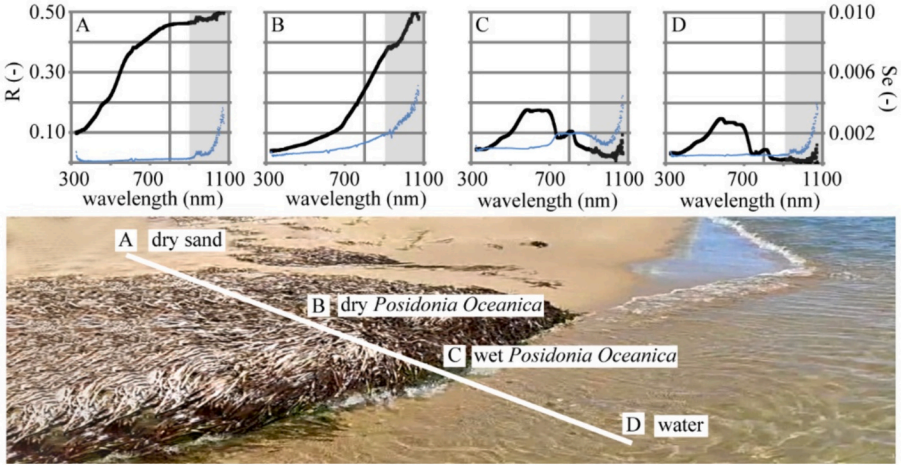

Fig. 9. Spectral signature of dry sand (A), dry P. oceanica (B) wet P. oceanica (C) and water (D), acquired at Torre Salsa beach.

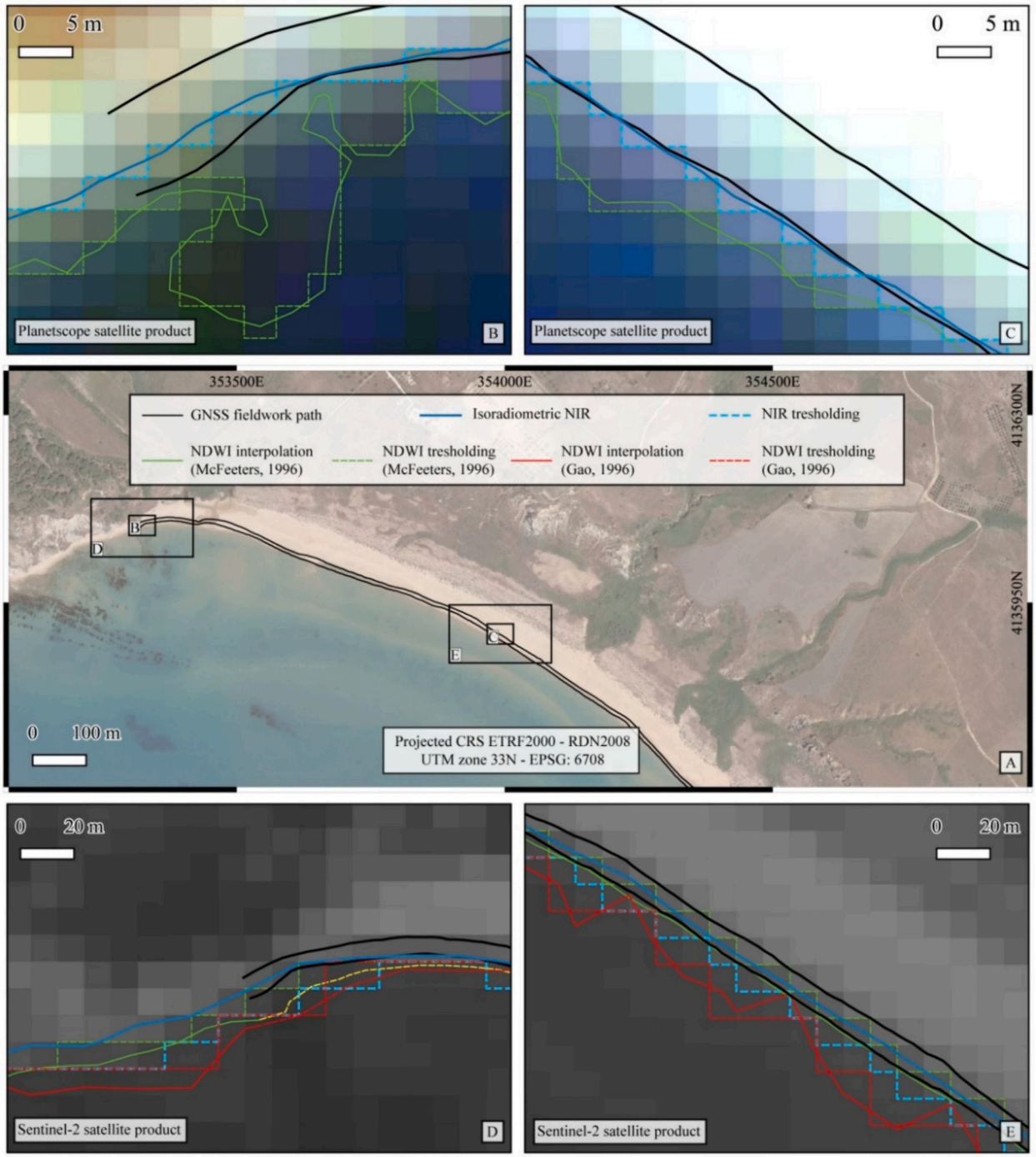

Fig. 10. Shoreline position extracted from different methods: In blue and dashed blue the "isoradiometric shoreline" and the "NIR thresholding shoreline", respectively; In green and red the NDWI are based on McFeeters (1996) and Gao (1996), with continuous lines where the shoreline is retrieved via interpolation and dashed lines where is retrieved via thresholding. Black lines represent the GNSS delimited positions of the beachface. Shorelines were extracted by PS images (B, C) and S2 images (D, E). (For interpretation of the references to colour in this figure legend, the reader is referred to the web version of this article.)

deviation, μ and σ, of the shoreline from the LTT.

Table 3 shows that the thresholding methods are less accurate than the interpolation method and that the use of NDWI formulations does not produce better results. Unexpectedly, the accuracy achieved by applying the isoradiometric method to S2 (~95%) is higher than that achieved with PS (65%), although in terms of μ and σ, the performance is better when applied on PS (0.65 and 0.42) than on S2 (0.94, 0.74). Unexpectedly, the accuracy obtained by applying the isoradiometric method on S2 (94%) is higher than that achieved with PS (65%). However, in terms of μ and σ, the performance is higher when applied to PS compared to S2 ($0.65 < 0.94$ m and $0.42 < 0.74$ m, respectively). Also, the use of McFeeters' formula on S2 yielded superior statistics compared to Gao's formula. This is likely due to the bands' resolution used in McFeeters' formula (10 m) being finer than that in Gao's formula (20 m). Additionally, it has been quantified whether a shoreline, evaluated by a threshold method (as shown in Fig. 11) prior to the application of a vector generalization algorithm and after it, retains or assumes the characteristic of isoradiometry. The threshold method was applied on the PS and S2 NIR bands, already referred to for the Torre Salsa test, with the threshold value selected as the minimum between

Table 3
Statistics characterizing the tested methods.

	Method	Accuracy (%)	μ (m)	σ (m)
Planetscope	NIR interpolation, isoradiometry	64.99	0.65	0.42
	NIR threshold	44.37	1.23	0.80
	NDWI interpolation (McFeeters, 1996)	8.38	4.09	3.17
	NDWI threshold (McFeeters, 1996)	12.46	4.29	3.28
Sentinel-2	NIR interpolation, isoradiometry	95.4	0.94	0.74
	NIR threshold	8.04	5.13	4.37
	NDWI interpolation (McFeeters, 1996)	66.6	1.09	3.77
	NDWI threshold (McFeeters, 1996)	5.98	2.08	4.99
	NDWI interpolation (Gao, 1996)	9.09	14.37	11.66
	NDWI threshold (Gao, 1996)	4.71	16.78	12.89

the two peaks representing water and land domains.

Quantitatively, it was found (Table 4) that a shoreline based on a threshold intersects the isoradiometric lines multiple times (6 in the PS test and 15 in the S2 test), even after the application of some vector generalization algorithms. Indeed, a subsequent vector generalization (or smoothing) would allow the line's pattern to resemble what can be observed in nature. Among the algorithms evaluated, the Snakes algorithm produced the most reliable results, with several intercepted isoradiometric curves less equal to the count intercepted before applying the generalization. The average distance between the first and last intercepted isoradiometric lines was 3–4 m on PS and 26–29 m on S2. The application of Snake algorithms also decreases the planimetric width of the intercepted isoradiometric lines.

6. Discussion

6.1. The significance of beach slope and sand grain size

The morphology of the sandy beach foreshore, which encompasses the section hosting the shoreline (Fig. 1), is predominantly influenced by the sand's grain size. In a minor way, it is shaped by various hydrodynamic processes such as wave action, impact, uprush, backwash, and in/exfiltration. These dynamic processes are regulated by the tidal regimes present in the area. Therefore, for this study, beaches with microtidal regimes were specifically chosen, to further minimize the impact of these processes on the foreshore morphology (Bujan et al., 2019). The beach grain size directly influences the slope of the foreshore, and these two variables are critical for the coastlines detection using radiometric measurements. This is due to the electromagnetic absorption of seawater across various spectrum wavelengths, which is a pivotal aspect of remote sensing (Clevers et al., 2008). Specifically, for a given length, such as the dimension of a pixel in a remotely sensed image, the slope of the seabed becomes an essential factor in determining the maximum thickness of the water column. This thickness, in turn, influences the water's absorption capacity and, the absorption capacity determines the maximum penetration depth of electromagnetic waves. For Sicilian sandy beaches, based on the diffuse attenuation coefficients proposed by Maltese et al., 2008, the penetration depth for NIR wavelengths is estimated to reach roughly 25 cm of water column (Fig. 6). The coastline detection through radiometric measurements is closely connected to the beach slope, and the beach sand grain size determines the slope. Furthermore, the penetration depth of electromagnetic waves, influenced by these physical characteristics, determines the smallest detectable change in elevation across the beach slope. Finer sands typically result in beaches with gentler slopes and a lesser elevation difference between the upstream and downstream parts of a pixel in satellite remote sensing imagery. Suppose the elevation difference within a pixel is less than or equal to the maximum penetration depth of seawater at NIR wavelengths. In that case, the spatial accuracy of shoreline extraction effectively becomes as precise as the pixel's geometrical resolution. Under these circumstances, any additional attempts to increase the accuracy of the shoreline extraction method would not yield significant improvements because the maximum precision allowed by the physics of the process used for the measurement has been achieved. As indicated in Table 1, the maximum penetration depth of seawater is a significant consideration for high geometric resolution satellite products, such as those from PS, when examining the three sandy beaches under study. This factor, however, does not have a marked impact on shoreline extraction from satellite datasets with mid-high to medium geometric resolution, like those from S2 and LS. For instance, at Torre Salsa Beach, with a seawater penetration depth estimated at around 25 cm, the applied methodology effectively reaches the limits of the maximum possible resolution. This is evident as the elevation difference for a PS pixel is measured at a mere 22 cm, nearly matching the water penetration depth. This closeness indicates that the spatial resolution of shoreline detection is at its peak capability, suggesting that any efforts to enhance the accuracy of the detection method might not yield significant improvements under these specific conditions.

6.2. The shoreline radiometric signature

The interpretation of diffuse attenuation coefficients by Maltese et al. (2008) suggests that the NIR and RE spectral bands generally enable the most accurate shoreline extraction. This is confirmed by our performance evaluation (see Fig. 7, Table 2 and SM Fig. 3 and Table 5–6), where these two bands exhibit comparable efficacy. Consistent with this, most shoreline extraction methods using earth observation data in the literature utilize the NIR band, which typically provides high contrast between land and water and is historically available across various satellite imaging platforms (Alicandro et al., 2019). Certainly, this applies to regions where the spatial consistency of other radiometric elements can be assumed. This aspect specifically pertains to the reflectance characteristics of the seabed and the optical properties of the water column, which are largely determined by the concentration of chlorophyll, suspended particles, and coloured dissolved organic matter. The reflectance from the sea bottom becomes increasingly significant in relation to the water depth moving from the nearshore towards the foreshore. The acquired foreshore radiometric signatures (Fig. 4 and 7A) highlight that the signature of the sand differs the water one, starting from 580 nm and moving towards longer wavelengths. In particular, the shoreline-related radiometric signature is characterized by an SR of wet sand that begins to exhibit similar properties to that of water, as indicated by the light red area in Fig. 5A and supported by radiometric profiles plotted in Fig. 5B. Interpreting the same data using an NDWI analogous expression, results highlight the position of the coastline where the normalized difference value between the two SR values converges towards zero.

6.3. Accuracy and limitations of the isoradiometric method

The shoreline extraction method presented in this study achieves sub-pixel resolution, as detailed in SM Tables 8 and 9. The results indicate that the shoreline accuracy obtained from LS-8 (with a pixel size of 30 m), S2 (pixel sizes of 10 and 20 m), and PS (pixel size of 3 m) are comparable, as shown in Table 1 and SM Tables 5 and 6. The standard deviation values in these tables can be interpreted as indicators of shoreline extraction accuracy. Remarkably, the sub-pixel resolution of this method enhances the resolution of the input images, potentially improving it by a factor of up to 11. An area for further refinement in the proposed method, highlighted in Fig. 8, is the interpolation approach. Currently, it struggles to accurately reproduce abrupt changes in shoreline direction which are more prevalent in human-altered coasts

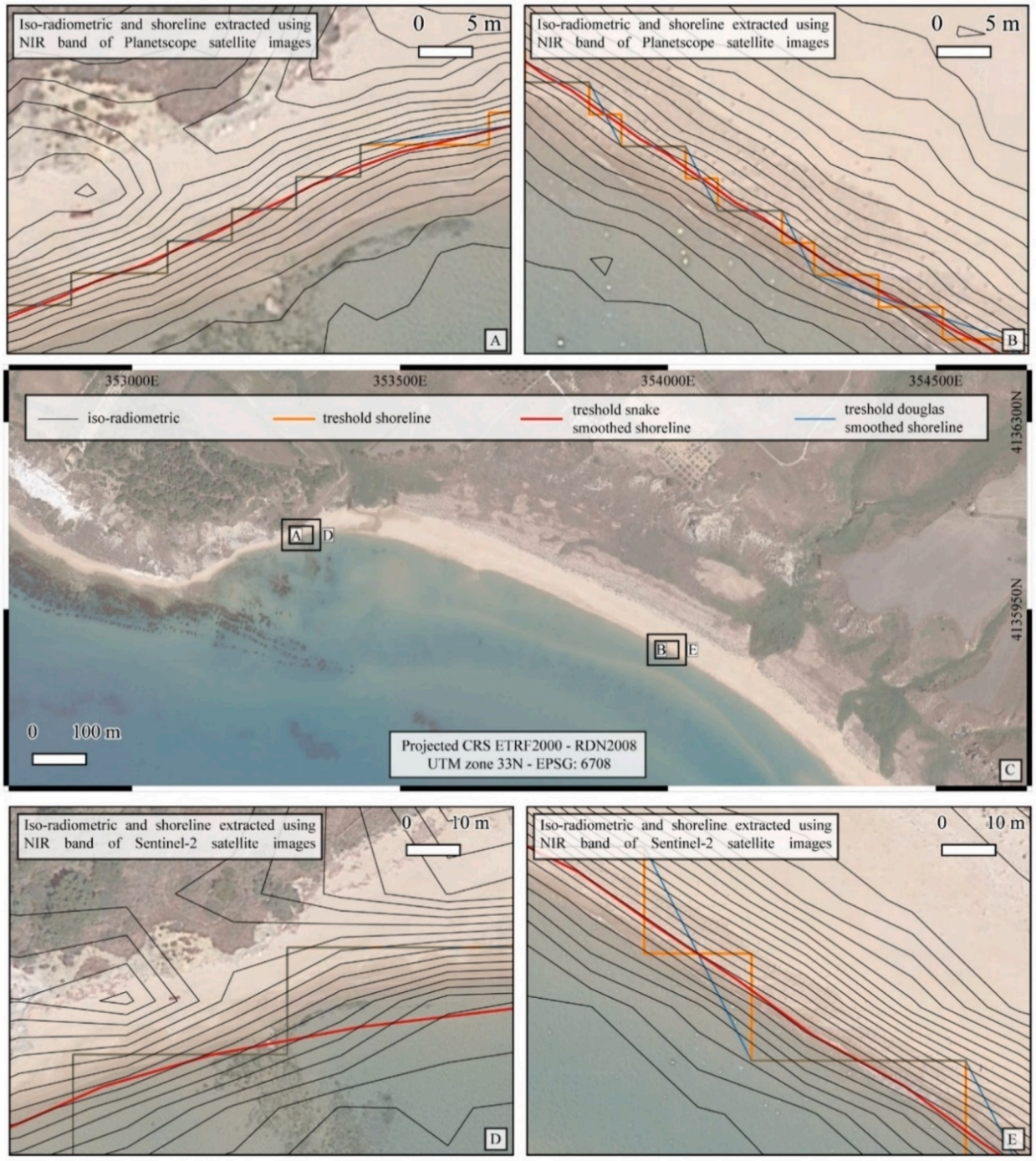

Fig. 11. Isoradiometric curves (black lines) and the shoreline estimated by applying a NIR band threshold. Thresholding shorelines (orange line) without any post-processing, along with the use of some vector generalization algorithms: the Snake (red line) and the Douglas (Cyan line). The test is conducted on an S2 image (D, E) and a PS image (B, C). (For interpretation of the references to colour in this figure legend, the reader is referred to the web version of this article.)

Table 4
Isoradiometric intercepted by shorelines assessed by thresholding without and with the application of some vector generalization algorithms.

	Isoradiometric step (−)	Vector generalization algorithm	Number of intercepted isoradiometric curves	Isoradiometric range (−)	Distance between first and last intercepted isoradiometric lines (m)
PS	0.02	none	6	0.14–0.24	4.28
		Snake	5	0.16–0.24	3.38
		Douglas	6	0.14–0.24	4.28
S2	0.02	none	15	0.04–0.32	26.65
		Snake	15	0.02–0.3	29.29
		Douglas	15	0.04–0.32	26.65

rather than natural settings. Furthermore, processing satellite images of different pixel-size resolutions demonstrated that this method could yield low average distances and standard deviations when compared to GNSS acquisitions, even using low-resolution satellite imagery, reaching up to an accuracy level of 95%, highlighting the method's effectiveness in various coastal environments and across different satellite platforms. While the proposed method for shoreline extraction demonstrates high performance, it does face some limitations, primarily due to varying reflectance values under different environmental conditions. As observed at Vendicari beach, the presence of a significant amount of beached *P. oceanica* dampens hydrodynamics, reducing the foreshore area affected by wave uprush (SM 3.1 and SM Table 5). The radiometric signature of dry *P. oceanica* displays a concavity opposite to that of dry sand (Fig. 11A and B), and the spectral signature of wet *P. oceanica* closely resembles that of water, posing challenges for radiometric discrimination. Despite this, the horizontal accuracy of the extracted shorelines at Vendicari beach, which uniquely featured *P. oceanica*, was encouragingly high and significantly finer than the pixel resolution of the satellite images used. Other sources of error (e.g. turbitidy (Maltese et al., 2013) are discussed in section 4.1 of SM.

Moreover, the variability in reflectance along the shoreline, as discussed by Maltese et al. (2006), may be attributed to the optical properties of the water column. Additionally, spatial variations in grain size can influence bottom reflectance and, consequently, the accuracy of remote sensing in shoreline detection. The relationship between mean grain size of beach sands and their spectral reflectance was demonstrated by Leu (1977). This model accounts for the spectral reflectance of particulate surfaces, incorporating physical properties like wavelength, refractive and absorption indices, grain size, packing density, and surface roughness. It postulates that total spectral bidirectional reflectance consists of a specular (surface) component and an internal (volume) component. When electromagnetic radiation strikes a granular surface, some is reflected specularly, while the rest penetrates the granules. Vincent and Hunt (1968) noted that with smaller grain sizes, surface radiation experiences more multiple reflections due to an increased number of particles per unit area, which generally leads to reduced surface reflectance as outlined by Emslie (1966). Conversely, for the volume component of reflectance, smaller grains mean the incident radiation interacts with more internal boundaries, having traversed less of the absorbing medium. Therefore, the volume component of reflectance tends to increase as grain size decreases. Thus, a positive correlation exists between the surface component of reflectance and grain size, while a negative correlation is seen with the volume component. It is also important to consider that beach sand predominantly comprises quartz grains. The presence of an iron-oxide coating on quartz grains is significant as it diminishes reflectance due to the coating's high absorption characteristics. However, in smaller study areas, the properties of the water column and the sand's reflectance tend to be more spatially consistent. As a result, the isoradiometric value delineating the remotely sensed shoreline, should maintain spatial consistency.

6.4. The comparison with literature methods

Fig. 10 and Table 3 show that outcomes of the proposed methodology compared with other shoreline extraction methods, is characterized by better accuracy (validated both quantitatively and through the GNSS survey) and are not characterized by the typical sawtooth morphology. We are aware that sawtooth shorelines resulting from pixel-bounded shoreline extraction methods could be smoothed to reach similar performances to the proposed method, but we believe that this practice further increases the abstraction level of the resulting shoreline. Increasing the processing phases in the shoreline extraction raises the difference of each digital number of the satellite product from the physical level of abstraction, that is, the natural reflected radiance. The utility of this smoothing step comes from the necessity to convert the elliptical areas of the projection of each steradian acquired by the sensor on the Earth's surface into square pixels through a gridding algorithm. Differently, the proposed methodology aims to do the opposite, moving from the logic level of abstraction (the gridded dataset) towards the physical level of abstraction and thus, not considering the square shape of each pixel, while just the centre of the sensed area. We believe it is closer to the reality to consider digital numbers as the reflected radiance from a small area whose centroid is represented by the pixel centre, and then interpolate instead of extending the information at the whole pixel surface, which could not correctly represent the actual shape of the surface reflecting the radiance. It is also important to note that the shoreline as defined by some widespread literature methods may not correspond to a radiometric value but instead represents a land-water boundary pixels clusters. In threshold-based approaches, the threshold value discriminates between pixels, but it does not inherently represent a radiometric value. Examining the band frequency histogram, the threshold is placed in a relatively flat area of minimum frequency between two peaks, hence the difference in reflectance between pixels on either side of the threshold can be significant.

7. Conclusions

We introduce an isoradiometric sub-pixel shoreline extraction method based on satellite earth observation and interpolation techniques. We conducted a thorough accuracy assessment by comparing our extracted shorelines with field GNSS acquisition surveys at three distinct sites along the Sicily coasts. This method enabled us to precisely define the spectral signature across a beach transect, determining that wavelengths ranging from 700 to 850 nm most accurately approximate the shoreline position. The effectiveness of this method was further validated through accuracy and horizontal displacement estimations of various satellite product bands, particularly RE and NIR, which demonstrated accuracy values exceeding 50%, with mean (μ) and standard deviation (σ) values remaining below 2 m. Additionally, sedimentological analyses were employed to determine the slope of the foreshore, allowing us to calculate the elevation difference for each geometric resolution of the satellite product's pixels. Our findings suggest that further efforts to enhance the accuracy of shoreline extraction methodologies may not yield significant improvements. A direct comparison with other methodologies indicates that our method improves the accuracy offering a robust and reliable means of shoreline extraction. To further validate the proposed methodology, it would be beneficial to conduct additional comparisons with algorithms based on image classification and indices, as well as applying it to benchmark datasets. Our in situ spectroradiometric measurements have shown that beached *P. oceanica* can significantly alter both the spectral signature and the dynamics of wave motion, leading to inaccuracies in the real shoreline position, as observed at Vendicari beach. Other identified challenges, such as shadows, marshes, breaking waves, and glints, can generally be mitigated by excluding satellite products affected by these issues from our analyses. Another issue is represented by a subpixel corregistration of the images and an improvement scheme of the satellite products' geometric accuracy should be evaluated to be integrated within a fully automated method. However, the full potential of our method in various contexts, especially in areas with high tidal oscillations, remains to be explored. The proposed shoreline extraction method holds significant promise for coastal management, particularly in the detection and mitigation of coastal erosion risks but also in extracting shoreline evolution time series, which can serve as valuable proxies for studying the impact of climate forcing on coastal landscape evolution.

CRediT authorship contribution statement

F. Caldareri: Writing – review & editing, Writing – original draft, Visualization, Validation, Software, Methodology, Investigation, Formal analysis, Data curation, Conceptualization. **A. Sulli:** Writing – review & editing, Writing – original draft, Supervision, Resources, Project

administration, Funding acquisition. **N. Parrino:** Conceptualization, Methodology, Software, Validation, Formal Analysis, Data curation, Visualization, Investigation, Writing original draft, Writing review, and editing. **G. Dardanelli:** Writing – review & editing, Investigation. **S. Todaro:** Writing – review & editing, Writing – original draft. **A. Maltese:** Writing – review & editing, Writing – original draft, Visualization, Validation, Supervision, Software, Methodology, Investigation, Formal analysis, Data curation, Conceptualization.

Funding

Partially funded by European Union - NextGenerationEU - Mission 4 "Education and Research" - Component 2 "From Research to Business" – Investment 3.1 "Fund for the realization of an integrated system of research and innovation infrastructures" - Project IR0000037 - GeoSciences IR.

Declaration of competing interest

The authors declare that they have no known competing financial interests or personal relationships that could have appeared to influence the work reported in this paper.

Data availability

Data will be made available on request.

Acknowledgements

Planetscope Dove and SuperDove images were made available by Planet Labs Inc. (San Francisco, CA, USA) within the Planet's Education and Research (E and R) Program.

Appendix A. Supplementary data

Supplementary data to this article can be found online at https://doi.org/10.1016/j.rse.2024.114286.

References

Alicandro, M., Baiocchi, V., Brigante, R., Radicioni, F., 2019. Automatic shoreline detection from eight-band VHR satellite imagery. J. Mar. Sci. Eng. 7, 459. https://doi.org/10.3390/jmse7120459.

Almeida, L.P., Efraim De Oliveira, I., Lyra, R., Scaranto Dazzi, R.L., Martins, V.G., Da Fontoura, Henrique, Klein, A., 2021. Coastal analyst system from space imagery engine (CASSIE): shoreline management module. Environ. Model Softw. 140, 105033 https://doi.org/10.1016/j.envsoft.2021.105033.

American Society for Testing and Materials, 2007. Annual Book of ASTM Standards, 1987 Annual Book of. ASTM Standards. ASTM.

Awada, H., Ciraolo, G., Maltese, A., Provenzano, G., Moreno Hidalgo, M.A., Còrcoles, J.I., 2019. Assessing the performance of a large-scale irrigation system by estimations of actual evapotranspiration obtained by Landsat satellite images resampled with cubic convolution. Int. J. Appl. Earth Obs. Geoinf. 75, 96–105. ISSN 1569-8432,. https://doi.org/10.1016/j.jag.2018.10.016.

Bagnold, R.A., 1940. Beach formation by waves: some model experiments in A wave tank. (Includes photographs). J. Instit. Civ. Eng. 15, 27–52. https://doi.org/10.1680/ijoti.1940.14279.

Bascom, W.M., 1951. The relationship between sand size and beach-face slope. Eos. Trans. AGU 32, 866–874. https://doi.org/10.1029/TR032i006p00866.

Bengoufa, S., Niculescu, S., Mihoubi, M.K., Belkessa, R., Abbad, K., 2023. Automatic detection of Hydrodynamical and biological indicators of the shoreline using a convolutional neural network. In: Niculescu, S. (Ed.), European Spatial Data for Coastal and Marine Remote Sensing. Springer International Publishing, Cham, pp. 191–205. https://doi.org/10.1007/978-3-031-16213-8_11.

Boussetta, A., Niculescu, S., Bengoufa, S., Mejri, H., Zagrarni, M.F., 2023. Assessment of coastal vulnerability to erosion risk using geospatial and remote sensing methods (Case of Jerba Island, Tunisia). In: European Spatial Data for Coastal and Marine Remote Sensing. Springer, Cham. https://doi.org/10.1007/978-3-031-16213-8_7.

Bujan, N., Cox, R., Masselink, G., 2019. From fine sand to boulders: examining the relationship between beach-face slope and sediment size. Mar. Geol. 417, 106012 https://doi.org/10.1016/j.margeo.2019.106012.

Chen, D., Huang, J., Jackson, T.J., 2005. Vegetation water content estimation for corn and soybeans using spectral indices derived from MODIS near- and short-wave infrared bands. Remote Sens. Environ. 98, 225–236.

Cipolletti, M.P., Delrieux, C.A., Perillo, G.M.E., Cintia Piccolo, M., 2012. Superresolution border segmentation and measurement in remote sensing images. Comput. Geosci. 40, 87–96. https://doi.org/10.1016/j.cageo.2011.07.015.

Clevers, J.G.P.W., Kooistra, L., Schaepman, M.E., 2008. Using spectral information from the NIR water absorption features for the retrieval of canopy water content. Int. J. Appl. Earth Observ. Geoinform. 10, 388–397. https://doi.org/10.1016/j.jag.2008.03.003.

Costantino, D., Pepe, M., Dardanelli, G., Baiocchi, V., 2020. Using optical satellite and aerial imagery for automatic coastline mapping. Geographia Technica 15. https://doi.org/10.21163/GT_2020.152.17.

Dardanelli, G., Maltese, A., 2022. On the accuracy of cadastral Marks: statistical analyses to assess the congruence among GNSS-based positioning and official maps. Remote Sens. 14, 4086. https://doi.org/10.3390/rs14164086.

Dardanelli, G., Maltese, A., Pipitone, C., Pisciotta, A., Lo Brutto, M., 2021. NRTK, PPP or static, that is the question. Testing different positioning solutions for GNSS survey. Remote Sens. 13 https://doi.org/10.3390/rs13071406.

Dean, R.G., 1991. Equilibrium Beach profiles: characteristics and applications. J. Coast. Res. 7 (1), 53–84. http://www.jstor.org/stable/4297805.

Douglas, D., Peucker, T., 1973. Algorithms for the reduction of the number of points required to represent a digitized line or its caricature. Cartographica: Int. J. Geogr. Inform. Geovisualiz. 10 (2), 112–122. https://doi.org/10.3138/FM57-6770-U75U-7727.

Emslie, A.G., 1966. Theory of diffuse spectral reflectance of a thick layer of absorbing and scattering particles. In: Heller, G.B. (Ed.), Thermosphysics and Temperature Control of' Spacecraft and Entry Vehicles, Progress in Astronautics and Aeronautics 18. Academic Press, New York.

Finkl, C.W., Makowski, C., 2020. Encyclopedia of Coastal Science. Encyclopdia of Earth Sciences Series. Springer, Cham. https://doi.org/10.1007/978-3-319-48657-4. ISSN: 1388-4360.

Gao, B., 1996. NDWI—A normalized difference water index for remote sensing of vegetation liquid water from space. Remote Sens. Environ. 58, 257–266. https://doi.org/10.1016/S0034-4257(96)00067-3.

Holmes, T.R.H., Poulter, B., McCorkel, J., Jennings, D.E., Wu, D.L., Efremova, B., Shiklomanov, A., Johnson, W.R., Jhabvala, M., Hook, S.J., 2024. On-orbit spatial performance characterization for thermal infrared imagers of Landsat 7, 8, and 9, ECOSTRESS and CTI. J. Geophys. Res. Biogeosci. 129, e2023JG007506 https://doi.org/10.1029/2023JG007506.

Jin, S., Wang, Q., Dardanelli, G., 2022. A review on multi-GNSS for earth observation and emerging applications. Remote Sens. 14, 3930. https://doi.org/10.3390/rs14163930.

Kass, M., Witkin, A., Terzopoulos, D., 1988. Snakes: active contour models. Int. J. Comput. Vis. 1, 321–331.

Leu, 1977. Visible and near- infrared reflectance of beach sands: A study on the spectral reflectance grain size relationship. Remote Sens. Environ. 6, 169–182.

Luijendijk, A., Hagenaars, G., Ranasinghe, R., Baart, F., Donchyts, G., Aarninkhof, S., 2018. The state of the World's beaches. Sci. Rep. 8, 6641. https://doi.org/10.1038/s41598-018-24630-6.

Maltese, A., Capodici, F., Ciraolo, G., Loggia, G.L., 2013. Coastal zone water quality: calibration of a water-turbidity equation for MODIS data. European Journal of Remote Sensing 46, 333–347. https://doi.org/10.5721/EuJRS20134619.

Maltese, A., La Loggia, G., Cox, E., Ciraolo, G., 2006. The classification of submerged vegetation using hyperspectral MIVIS data. Ann. Geophys. https://doi.org/10.4401/ag-3152.

Maltese, A., Pampalone, V., Malthus, T., Ciraolo, G., Karpouzli, E., la Loggia, G., 2008. Processing of field spectroradiometric data for remote sensing mapping of submerged vegetation in coastal zones and lagoon environments. EARSeL eProceedings 7, 105–119.

Maltese, A., Caldareri, F., Parrino, N., Todaro, S., Dardanelli, G., Sulli, A., 2023. A radiometric contouring approach to map the shoreline. In: Remote Sensing for Agriculture, Ecosystems, and Hydrology XXV. Presented at the Remote Sensing for Agriculture, Ecosystems, and Hydrology XXV. SPIE, pp. 57–66. https://doi.org/10.1117/12.2690731.

Malik, J.N., Srivastava, E., Gadhavi, M.S., Livio, F., Sharma, N., Arora, S., Sulli, A., 2024. Holocene surface-rupturing paleo-earthquakes along the Kachchh Mainland Fault: shaping the seismic landscape of Kachchh, Western India. Scientific Reports 14 (1), 11612.

Maltese, A., Caldareri, F., Dardanelli, G., Todaro, S., Parrino, N., Sulli, A., 2024. On the shoreline positioning via remote sensing imagery: an isoradiometric approach. J. Appl. Remote. Sens. 18, 014529 https://doi.org/10.1117/1.JRS.18.014529.

Masselink, G., Puleo, J.A., 2006. Swash-zone morphodynamics. Cont. Shelf Res. 26, 661–680. https://doi.org/10.1016/j.csr.2006.01.015.

McFeeters, S.K., 1996. The use of the normalized difference water index (NDWI) in the delineation of open water features. Int. J. Remote Sens. 17 (7), 1425–1432. https://doi.org/10.1080/01431169608948714.

Otsu, N., 1979. A threshold selection method from gray-level histograms. IEEE Trans. Syst. Man, Cybern. 9, 62–66. https://doi.org/10.1109/TSMC.1979.4310076.

Palomar-Vázquez, J., Almonacid-Caballer, J., Pardo-Pascual, J., Elena, Sánchez-García, 2018. Shorex: a new tool for automatic and massive extraction of shorelines from landsat and sentinel 2 imagery.

Pardo-Pascual, J., Almonacid-Caballer, J., Ruiz, Palomar-Vázquez, 2012. Automatic extraction of shorelines from Landsat TM and ETM multi-temporal images with subpixel precision. Remote Sens. Environ. 123, 1–11. https://doi.org/10.1016/j.rse.2012.02.024.

Parrino, N., Pepe, F., Burrato, P., Dardanelli, G., Corradino, M., Pipitone, C., Morticelli, M.G., Sulli, A., Di Maggio, C., 2022. Elusive active faults in a low strain

rate region (Sicily, Italy): hints from a multidisciplinary land-to-sea approach. Tectonophysics 839, 229520. https://doi.org/10.1016/j.tecto.2022.229520.
Parrino, N., Burrato, P., Sulli, A., Gasparo Morticelli, M., Agate, M., Srivastava, E., Malik, J.N., Di Maggio, C., 2023. Plio-quaternary coastal landscape evolution of North-Western Sicily (Italy). J. Maps 1–13. https://doi.org/10.1080/17445647.2022.2159889.
Prewitt, J., Mendelsohn, M.L., 1965. The analysis of cell images. Ann. N. Y. Acad. Sci. 128 (3), 1035–1053. https://doi.org/10.1111/j.1749-6632.1965.tb11715, 1, 2.2.
Short, A.D., 1999. Handbook of Beach and Shoreface Morphodynamics. John Wiley, Great Britain. ISBN 0-471-96570-7.
Srivastava, E., Malik, J.N., Parrino, N., Burrato, P., Sharma, N., Gadhavi, M., Sulli, A., Di Maggio, C., Morticelli, M.G., 2023. Extremely fast Holocene coastal landscape evolution in the Kachchh Upland (NW India): clues from a multidisciplinary review. J. Maps 1–10. https://doi.org/10.1080/17445647.2023.2167617.
Studley, Heather, Weber, Keith T., 2011. Comparison of image resampling techniques for satellite imagery. In: Final report: assessing post-fire recovery of sagebrush-steppe rangelands in southeastern Idaho, pp. 185–195. https://giscenter.isu.edu/research/Techpg/nasa_postfire/pdf/Ch15.pdf.
Terry, J.P., Goff, J., 2014. Megaclasts: proposed revised nomenclature at the coarse end of the Udden-Wentworth grain-size scale for sedimentary particles. J. Sediment. Res. 84, 192–197. https://doi.org/10.2110/jsr.2014.19.
Todaro, S., Agosta, F., Parrino, N., Cavalcante, F., Di Stefano, P., Giarrusso, R., Tondi, E., 2022. Fracture stratigraphy and oil first migration in Triassic shales, Favignana Island, western Sicily, Italy. Marine and Petroleum Geology 135, 105400.
Vincent, R.K., Hunt, G.R.I., 1968. Infrared reflectance from mat surfaces. Appl. Opt. 7 (1), 53–59.
Vos, K., Splinter, K., Palomar-Vázquez, J., Pardo-Pascual, J., Cabezas-Rabadán, C., Almonacid-Caballer, J., Kras, E., Luijendijk, A., Calkoen, F., Almeida, L., Pais, D., Klein, A., Mao, Y., Harris, D., Castelle, B., Buscombe, D., Vitousek, S., 2023. Satellite-derived shorelines for monitoring of sandy beaches: a benchmark study (preprint). Civ. Environ. Eng. https://doi.org/10.31223/X58W98.
Walker, R., 1992. Wave-and Storm-Dominated Shallow Marine Systems.